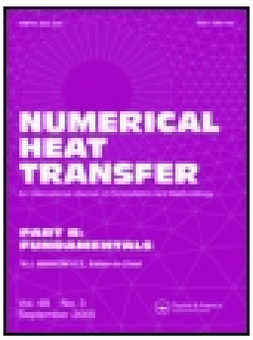

Taylor & Francis
Taylor & Francis Group

Numerical Heat Transfer: Part B: Fundamentals

ISSN: 1040-7790 (Print) 1521-0626 (Online) Journal homepage: https://www.tandfonline.com/loi/unhb20

TREATMENT OF THE INLET BOUNDARY CONDITIONS IN NATURAL-CONVECTION FLOWS IN OPEN-ENDED CHANNELS

Francisco Marcondes, Clovis R. Maliska

To cite this article: Francisco Marcondes, Clovis R. Maliska (1999) TREATMENT OF THE INLET BOUNDARY CONDITIONS IN NATURAL-CONVECTION FLOWS IN OPEN-ENDED CHANNELS, Numerical Heat Transfer: Part B: Fundamentals, 35:3, 317-345, DOI: 10.1080/104077999275893

To link to this article: https://doi.org/10.1080/104077999275893

Numerical Heat Transfer, Part B, 35:317–345, 1999

1040–7790/99 $12.00 + .00

TREATMENT OF THE INLET BOUNDARY CONDITIONS IN NATURAL-CONVECTION FLOWS IN OPEN-ENDED CHANNELS

Francisco Marcondes
Mechanical Engineering Department, Federal University of Paraíba, P.O. Box 100.69, 58109-970, Campina Grande, Brazil

Clovis R. Maliska
Mechanical Engineering Department, Federal University of Santa Catarina, P.O. Box 476, 88040-900, Florianópolis, SC, Brazil

The present work deals with the numerical solution of elliptic flows encountered in open-ended channels. The important question of applying boundary conditions for pressure and velocity for these flows is considered and a new method for the application of boundary conditions at the channel inlet is proposed. It is shown that the flow reversal at the channel outlet, which appears when nonsymmetric flow conditions are present, is strongly dependent on the entrance boundary conditions for pressure. Results for the straight channel in situations where flow reversal is present are reported for a wide range of Rayleigh numbers. Solutions for L-shaped channels are also reported with the aim of demonstrating the application of the model to arbitrary channels. It is shown that for certain flow situations the use of an elliptic formulation is imperative in order to predict correctly the flow behavior in open-ended channels.

INTRODUCTION

Natural-convection heat transfer in open-ended channels is encountered in a large number of engineering applications, as in the cooling of electronic equipments, solar collectors, grain drying equipments, room cooling/heating by passive systems, heat transfer in the condenser of domestic refrigerators, etc. A large body of the literature is related to the solution of the flow in straight vertical channels formed by two parallel vertical walls using the parabolic model. One of the pioneering works in this area is due to Bodoia and Oesterle [1] solving the natural-convection flow, using a parabolic model, for isothermal vertical walls. The calculated Nusselt numbers agreed well with the results of Elenbass [2]. Using the same parabolic model as employed in [1], Aung [3] solved the problem for both isothermal walls and prescribed heat flux conditions, and they also reported experimental results to validate the numerical model. Symmetric and nonsymmetric situations were investigated, and for the nonsymmetric situations they did not report the appearance of flow reversal at the outlet section in the range of Rayleigh numbers studied.

Received 13 January 1998; accepted 25 August 1998.
Address correspondence to Dr. Clovis R. Maliska, Mechanical Engineering Department, Federal University of Santa Catarina, P.O. Box 476, 88040-900 Florianópolis, SC, Brazil. E-mail: maliska@sinmec.ufsc.br

NOMENCLATURE

A	coefficients in the momentum, energy, and pressure equations
A_p^*	central coefficient for volume P without the transient term
B	source term for the pressure equation
c_p	specific heat at constant pressure
C_1, C_2, C_4	transformed diffusion coefficients
E	time-step multiplier
g	gravity acceleration
Gr	Grashof number
H	length of heated wall
J	Jacobian of the transformation
k	thermal conductivity
$L[\ ]$	denotes numerical approximation of the term inside the brackets
$\dot{m}$	mass flow ratio
Nu	Nusselt number
P	Pressure in excess
P_i	Inlet pressure
Pr	Prandtl number
$\hat{P}^\phi$	transformed pressure source term in the equation for ϕ
q''	heat flux in the heated wall
$\overline{q''}$	average heat flux in the heated wall
Ra	Rayleigh number
S	channel width
$\hat{S}^\phi$	transformed source term in the equation for ϕ
t	time
T	temperature
u, v	Cartesian components of the velocity vector
U, V	contravariant components of the velocity vector
$\hat{U}, \hat{V}$	auxiliar velocity components
$\overline{V}_i$	average velocity at the channel entrance
x, y	coordinates in the Cartesian system
α, β, γ	components of the metric tensor
$\overline{\alpha}, \overline{\beta}$	coefficients in the WUDS scheme
$\overline{\overline{\alpha}}$	thermal diffusivity
$\overline{\overline{\beta}}$	thermal expansion coefficient
Γ	general diffusion coefficient
$\overline{\overline{\mu}}$	absolute viscosity
$\overline{\overline{\nu}}$	kinematic viscosity
ρ	density
ξ, η	coordinates in the general curvilinear system
ϕ	scalar field
Ψ	streamlines

Subscripts

a	denotes Nusselt number computed in the heated wall
b	denotes Nusselt number computed using the difference between the convective and diffusive flows at the channel inlet and outlet
e, w, n, s, e', v'	denotes control-volume interfaces
exp	denotes experimental value
H	denotes parameter based on the heated length of the channel
i	denotes values at channel entrance or at the center of the control volume
L	denotes local values
max	denotes maximum value
o	denotes outside the channel
$P, E, W, N, S, NE, SE, NW, SW$	denotes the central control volume and neighbors
qs	denotes parameters based on the average heat flux
R	denotes reference values
S	denotes parameters based on the channel width
w	denotes parameters evaluated at the heated wall
ξ, η	partial derivates of first order
1	denotes parameters evaluated with $P_i = 0$
2	denotes parameters evaluated with P_i from Bernoulli's equation

Superscripts

n	denotes quantities evaluated at the nth time level
*	denotes dimensionless parameters

Sparrow et al. [4] analized the natural-convection flow in straight vertical channels with one isothermal wall and the other one insulated. Experimental results are shown for water for $(S/H)\,\mathrm{Ra}_s$ in the range of 2×10^2–10^5, and for four values of S/H, where S is the channel width and H its length. In spite of using a parabolic model, the numerical results agree well with the experimental ones, but, again, there is no capture of the existing recirculating flow closed to the cold wall at the channel exit. Aung and Worku [5] analyzed numerically, using the parabolic formulation, the mixed convection in vertical channels with different temperatures at the walls. For those cases in which the ratio between the Rayleigh and Reynold number was bigger than 250, the presence of a reversal flow at the channel outlet, close to the colder wall, was noted. However, for ratios bigger than 250, the solution became unstable after the recirculating region, so the marching procedure could not be employed after that region.

Only a few methodologies available in the literature also consider the flow elliptic in the streamwise direction. Kettleborough [6] solved the elliptic problem for the straight vertical channel with the same temperature prescribed at the walls, using the vorticity-stream function formulation. To bypass the fact that vorticity and stream function values are not known at the channel inlet and outlet, they extended the domain and applied zero normal derivatives at the extended boundary for all variables. Figure 1 shows the physical and the extended domain used in [6]. It is possible to observe that the extended domain is 1,800 times bigger than the physical domain. Therefore, the domain extension is not an attractive numerical alternative, since too many points are added to the linear systems of equation, increasing the computational effort considerably. Nakamura et al. [7] also solved the elliptic problem in the main flow direction using the formulation in terms of the stream function and vorticity with the same extended domain as used in [6]. In the work of Nakamura et al. [7] was proposed an equation for pressure, which must be satisfied according to the buoyancy forces. When vorticity and streamlines do not satisfy this equation, a new iteration is necessary. Naylor et al. [9] solved the natural-convection flow in straight channels using finite elements and primitive variables. They employed an elliptic formulation with the boundary conditions at the inlet based on the Jeffrey-Hamel flow. The strategy of extending the domain at the inlet was also used.

Nieckele and Azevedo [8] solved the straight-channel flow problem with one wall at a prescribed temperature and the other one insulated. They presented numerical and experimental results, with the former ones obtained by elliptic and parabolic precedures. Maliska and Marcondes [10], employing the elliptic formulation, solved the vertical flow in a straight channel, reporting the flow reversal at the channel exit.

In this work the methodology proposed by Maliska and Marcondes [10] is used to solve the natural-convection problem in arbitrary open-ended channels, writing the conservation equations in a generalized system of coordinates. Results obtained for the straight vertical channel are compared with numerical and experimental data available in the literature. The methodology is also applied for the solution of the natural-convection flow in an L-shaped channel, demonstrating the ability of the method to treat flows in arbitrary open-ended channels. The results are presented for prescribed heat flux and temperature, for air and water. A

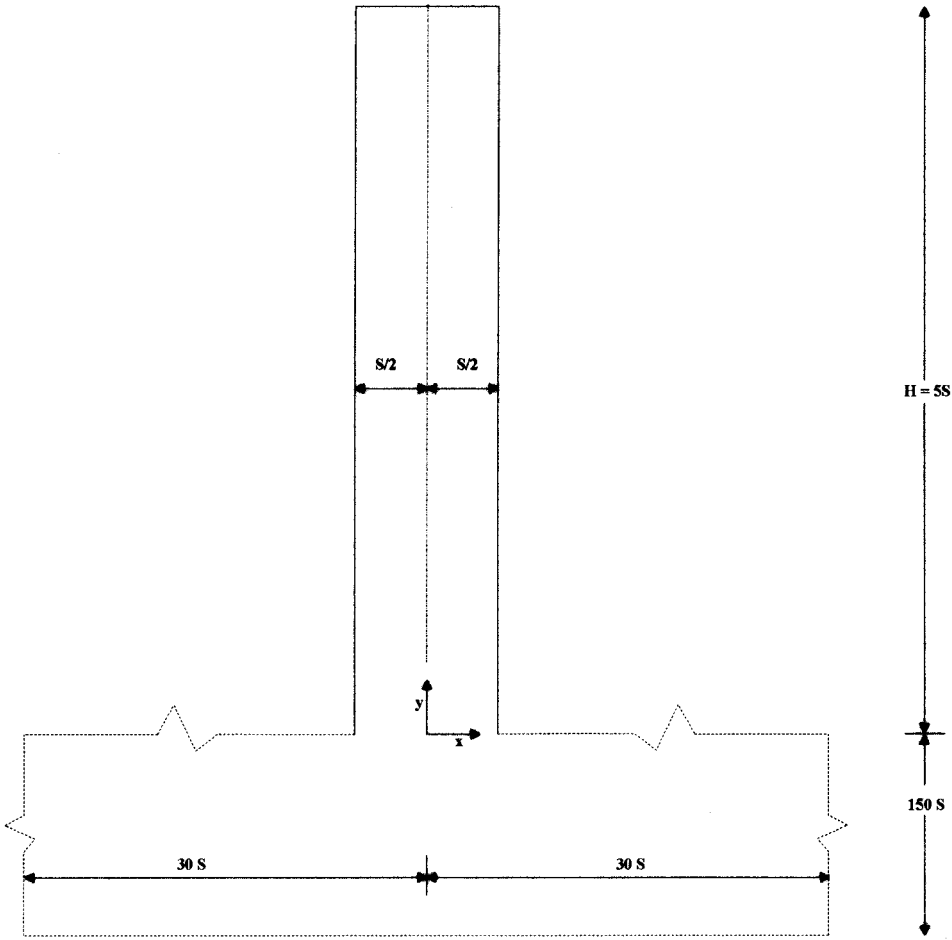

Figure 1. Physical and extended domain used by Kettleborough [6].

detailed discussion of how to apply boundary conditions at the inlet and their influence on the velocity field and heat transfer rate is presented.

MATHEMATICAL FORMULATION

The parabolic approximation is used extensively in the simulation of fluid flow problems due to the considerable savings in storage and computer time. It allows one to march in the streamwise direction, since diffusion of momentum and

heat are neglected in this direction, eliminating the need to obey boundary conditions downstream of the flow. This technique is used extensively for the solution of natural convection in straight vertical channels because it allows one to prescribe velocity and pressure at the entrance and to stop the marching procedure when the pressure excess is equal to zero. This position identifies the channel height that is able to drive the prescribed flow naturally. In this case the parabolic approximation helps to bypass the need to prescribe velocity and pressure, since they are unknown at the channel inlet.

However, when the channel height is given and the unknown is the mass flow rate that the channel is able to drive, the parabolic technique is no longer suitable and becomes iterative, resembling an elliptic segregated procedure. Furthermore, when arbitrary channels are involved it may by not possible to neglect the diffusion of momentum and energy in any direction, an elliptic procedure being required for the solution. Flow reversal may occur even for the straight channel with nonsymmetric boundary conditions at the walls, precluding the use of the parabolic approximation.

Therefore, if general conditions of natural-convection flows are to be simulated, it seems appropriate to develop efficient elliptic algorithms. The key question arising when using the full elliptic equations is the boundary conditions applicable at the channel entrance. If pressure is not imposed correctly at the inlet, the mathematical model will simulate a mixed-convection flow. If, for example, the level of pressure imposed as boundary condition is higher than the level created by the natural flow, the resulting flow will be of mixed type (natural/forced), causing an overestimation of the mass flow rate. This may inhibit the appearance of recirculating flows, as will be shown later when the numerical results are presented.

Therefore, the problem under consideration in this work is the numerical solution of two-dimensional laminar natural-convection flows in arbitrary channels, as depicted in Figure 2, where an L-shaped channel is shown. Considering laminar and incompressible flow, Boussinesq approximation, and Newtonian fluid, the following equations, written in a generalized curvilinear coordinate system, (ξ, η) [11] model the natural-convection flow:

$$\frac{\partial}{\partial \xi}(\rho U) + \frac{\partial}{\partial \eta}(\rho V) = 0 \tag{1}$$

$$\begin{aligned} \frac{1}{J}\frac{\partial}{\partial t}(\rho u) + \frac{\partial}{\partial \xi}(\rho U u) + \frac{\partial}{\partial \eta}(\rho V u) \\ = \frac{\partial}{\partial \xi}\left(C_1 \frac{\partial u}{\partial \xi}\right) + \frac{\partial}{\partial \eta}\left(C_4 \frac{\partial u}{\partial \eta}\right) + \frac{\partial}{\partial \xi}\left(C_2 \frac{\partial u}{\partial \eta}\right) \\ + \frac{\partial}{\partial \eta}\left(C_2 \frac{\partial u}{\partial \xi}\right) - \hat{P}^u + \hat{S}^u \end{aligned} \tag{2}$$

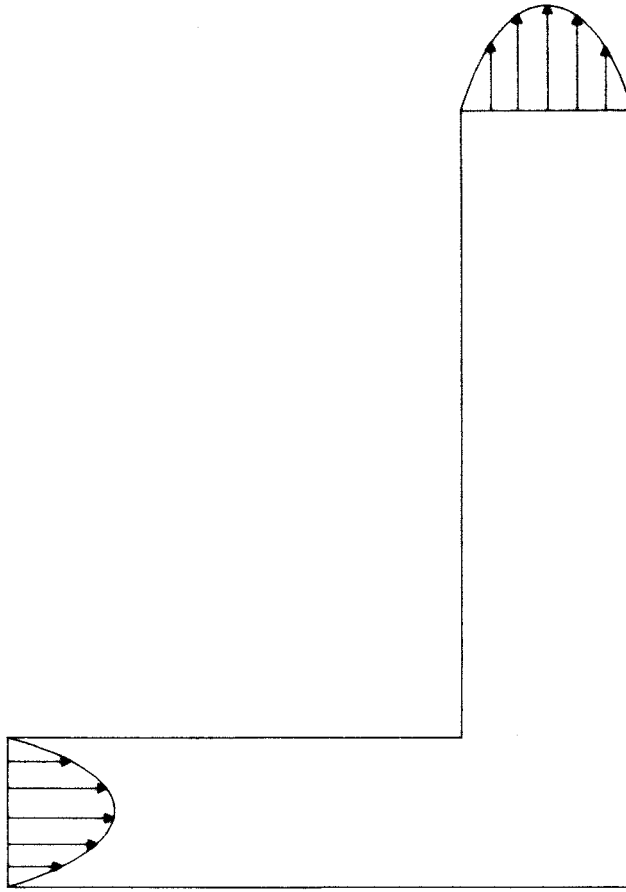

Figure 2. L-shaped channel under consideration.

$$\frac{1}{J}\frac{\partial}{\partial t}(\rho v)+\frac{\partial}{\partial \xi}(\rho U v)+\frac{\partial}{\partial \eta}(\rho V v)$$
$$=\frac{\partial}{\partial \xi}\left(C_1\frac{\partial v}{\partial \xi}\right)+\frac{\partial}{\partial \eta}\left(C_4\frac{\partial v}{\partial \eta}\right)+\frac{\partial}{\partial \xi}\left(C_2\frac{\partial v}{\partial \eta}\right)$$
$$+\frac{\partial}{\partial \eta}\left(C_2\frac{\partial v}{\partial \xi}\right)-\hat{P}^v+\hat{S}^v \tag{3}$$

$$\frac{1}{J}\frac{\partial}{\partial t}(\rho T)+\frac{\partial}{\partial \xi}(\rho U T)+\frac{\partial}{\partial \eta}(\rho V T)$$
$$=\frac{\partial}{\partial \xi}\left(C_1\frac{\partial T}{\partial \xi}\right)+\frac{\partial}{\partial \eta}\left(C_4\frac{\partial T}{\partial \eta}\right)+\frac{\partial}{\partial \xi}\left(C_2\frac{\partial T}{\partial \eta}\right)+\frac{\partial}{\partial \eta}\left(C_2\frac{\partial T}{\partial \xi}\right)+\hat{S}^T \tag{4}$$

where

$$
\begin{aligned}
\hat{P}^{\phi} &= \frac{P^{\phi}}{J} & \hat{S}^{\phi} &= \frac{S^{\phi}}{J} \\
C_1 &= \alpha J \Gamma^{\phi} & C_2 &= -\beta J \Gamma^{\phi} \\
C_4 &= \gamma J \Gamma^{\phi} & U &= y_{\eta} u - x_{\eta} v \\
V &= x_{\xi} v - y_{\xi} u & \alpha &= x_{\xi}^2 + y_{\xi}^2 \\
\beta &= x_{\xi} x_{\eta} + y_{\xi} y_{\eta} & \gamma &= x_{\eta}^2 + y_{\eta}^2 \\
P^{u} &= \frac{\partial P}{\partial \xi} y_{n} - \frac{\partial P}{\partial \eta} y_{\xi} & P^{v} &= \frac{\partial P}{\partial \eta} x_{\xi} - \frac{\partial P}{\partial \xi} x_{\eta} \\
S^{v} &= \frac{\rho g \overline{\overline{\beta}}}{J} (T - T_0) & S^{u} &= S^{T} = 0
\end{aligned}
\tag{5}
$$

Eqs. (1)–(4) may be written for a scalar ϕ as

$$
\begin{aligned}
&\frac{1}{J} \frac{\partial}{\partial t} (\rho \phi) + \frac{\partial}{\partial \xi} (\rho U \phi) + \frac{\partial}{\partial \eta} (\rho V \phi) \\
&\quad = \frac{\partial}{\partial \xi} \left(C_1 \frac{\partial \phi}{\partial \xi} \right) + \frac{\partial}{\partial \eta} \left(C_4 \frac{\partial \phi}{\partial \eta} \right) + \frac{\partial}{\partial \xi} \left(C_2 \frac{\partial \phi}{\partial \eta} \right) \\
&\qquad + \frac{\partial}{\partial \eta} \left(C_2 \frac{\partial \phi}{\partial \xi} \right) - \hat{P}^{\phi} + \hat{S}^{\phi}
\end{aligned}
\tag{6}
$$

When ϕ is equal to 1 one obtains the mass conservation equation, and for ϕ equal to u, v, and T, the momentum and the energy equations are recovered. Since only steady-state solutions are of interest, the transient term in the momentum conservation and energy equations are used for the iteration procedure.

NUMERICAL PROCEDURE

Figure 3 shows the elemental control volume used to integrate Eq. (6) in space and time to obtain the finite-volume approximation of the conservation equations. The grid layout employed is also depicted in the same figure. In this procedure the u and v velocities are both stored at each interface of a pressure control volume. This means that the elemental control volumes for u (or v) overlap each other, covering twice the computational domain. This layout avoids the problem encountered when the control volumes rotate relative to each other in the computational domain and only u is stored at the east and west faces and only v at the north and south faces. When this situation occurs the pressure gradient is evaluated with different levels of accuracy for the same dependent variable. On the

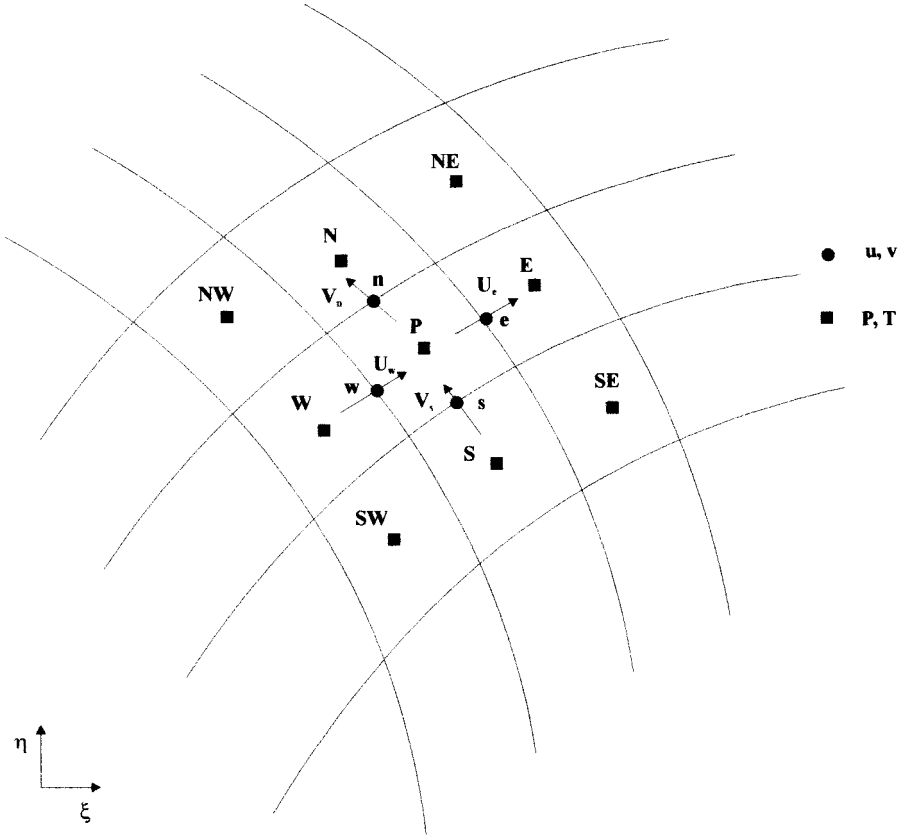

Figure 3. Elemental control volume and grid layout.

other hand, because of the overlapping control volumes for u and v, if an implicit solution for u and v is adopted, the solution of larger linear systems of equations will be required, increasing considerably the computational effort to obtain the solution. Therefore, the grid layout used here may not be efficient if an explicit solution for u and v is not used.

In this article the PRIME (PRessure Implicit, Momemtum Explicit) method [11, 12] is used and, due to its explicit solution for u and v, it keeps the computational effort for the solution of u and v to a minimum. Recent results [13], obtained using the PRIME method for different fluid flow problems in nonorthogonal coordinates, demonstrated that it is highly stable, showing that the allowable time step for convergence is, in general, very large, avoiding the need for searching the optimum, a task that may take considerable computational effort, sometimes overwhelming the computer savings due to the use of an implicit solution for u and v. Moreover, the PRIME method can be embodied in vectorized algorithms, taking advantage of the high degree of vectorization of explicit schemes [14].

Integrating Eq. (6) in space and time and using the WUDS scheme [15], with expressions for ϕ and its derivatives given by

$$\phi_e = \left(\frac{1}{2} + \alpha_e\right)\phi_P + \left(\frac{1}{2} - \alpha_e\right)\phi_E \tag{7}$$

$$\Gamma^\phi \left.\frac{\partial \phi}{\partial x}\right|_e = \overline{\beta}_e \Gamma_e^\phi \left(\frac{\phi_E - \phi_P}{\Delta \xi}\right) \tag{8}$$

with α and β obtained from the solution of the one-dimensional convection/diffusion problem, one obtains the algebraic equation for the general variable ϕ as

$$A_P \phi_P^{n+1} = \sum_{i=1}^{nb} A_i \phi_i^{n+1} - L[\hat{P}^\phi] + L[\hat{S}^\phi] + \frac{A_P \phi_P^n}{1 + E} \tag{9}$$

where $L[\ ]$ means the numerical approximation of the term inside the brackets and E is the time step normalized with respect to the maximum allowable time step in an explicit formulation [16].

EQUATION FOR PRESSURE

As usual when solving incompressible flows using segregated approaches, the equation for pressure is obtained by inserting the velocity-correction equations into the mass conservation equation. In the PRIME method the velocity-correction equations are the momentum equations written for the contravariant velocity components U and V, obtained by manipulating the approximate equations for u and v. These equations are given by

$$U_P = \hat{U}_P - \left(\frac{\alpha \Delta V}{A_P^u} \frac{\Delta P}{\Delta \xi}\right) + \left(\frac{\beta \Delta V}{A_P^u} \frac{\Delta P}{\Delta \eta}\right) \tag{10}$$

$$V_P = \hat{V}_P - \left(\frac{\gamma \Delta V}{A_P^v} \frac{\Delta P}{\Delta \eta}\right) + \left(\frac{\beta \Delta V}{A_P^v} \frac{\Delta P}{\Delta \xi}\right) \tag{11}$$

where $\hat{U}_P$ and $\hat{V}_P$ contain all terms of the momentum equation but the pressure gradients, and are given by

$$\hat{U}_P = \left(\frac{\sum_{i=1}^{nb} A_i u_i^{n+1}}{A_P} + \frac{u_P^n}{1 + E}\right) y_{\eta P} - \left(\frac{\sum_{i=1}^{nb} A_i v_i^{n+1}}{A_P} + \frac{v_P^n}{1 + E}\right) x_{\eta P} \tag{12}$$

$$\hat{V}_P = \left(\frac{\sum_{i=1}^{nb} A_i v_i^{n+1}}{A_P} + \frac{v_P^n}{1 + E}\right) x_{\xi P} - \left(\frac{\sum_{i=1}^{nb} A_i u_i^{n+1}}{A_P} + \frac{u_P^n}{1 + E}\right) y_{\xi P} \tag{13}$$

Inserting Eqs. (10) and (11) into the discretized mass conservation equation written for the contravariant velocity components given by

$$(U_e - U_w)\,\Delta\xi + (V_n - V_s)\,\Delta\eta = 0 \tag{14}$$

one obtains the following equation for pressure:

$$A_P P_P^{n+1} = \sum_{i=1}^{nb} A_i P_i^{n+1} + \nabla \cdot \overline{\mathbf{U}} \tag{15}$$

SOLUTION PROCEDURE

The steps to be followed to obtain the converged solution are as follows:

1. Estimate the initial fields of u, v, P, and T.
2. Calculate coefficients for the u- and v-momentum equations.
3. Calculate the $\hat{U}$ and $\hat{V}$ contravariant velocities. Recognize that in this step the explicit solution for momentum is realized.
4. Solve for pressure using Eq. (15).
5. Compute U and V, through Eqs. (10) and (11).
6. Compute the V velocity in the east and west faces by averaging the nearest V velocities that satisfy mass. The same procedure is applied to compute U in the north and south faces.
7. With U and V in each face, calculate u and v.
8. Calculate temperature.
9. Iteration back to step 2 is necessary to handle nonlinearities and interequation coupling.

Other internal cycles can be introduced in the above solution procedure, if desired. For example, the buoyancy source term in the momentum equation for the v-velocity component can be updated independently of the coefficients updating, which may result in better treatment of the velocity/temperature coupling in natural-convection flows.

BOUNDARY CONDITIONS

Boundary Conditions for Velocity

As outlined previously, when solving elliptic natural-convection flows for a specified channel height, the mass flow at the inlet is unknown. The strategy proposed in this article is to create an equation for the entrance velocity, considering this velocity as unknown. The pressure, in turn, needs to be specified at the entrance to form the pressure gradient term for the unknown entrance velocity. Figure 4 shows the half control volume used to integrate the momentum equation. Integrating Eq. (6) in space and time, and using the already known approximations

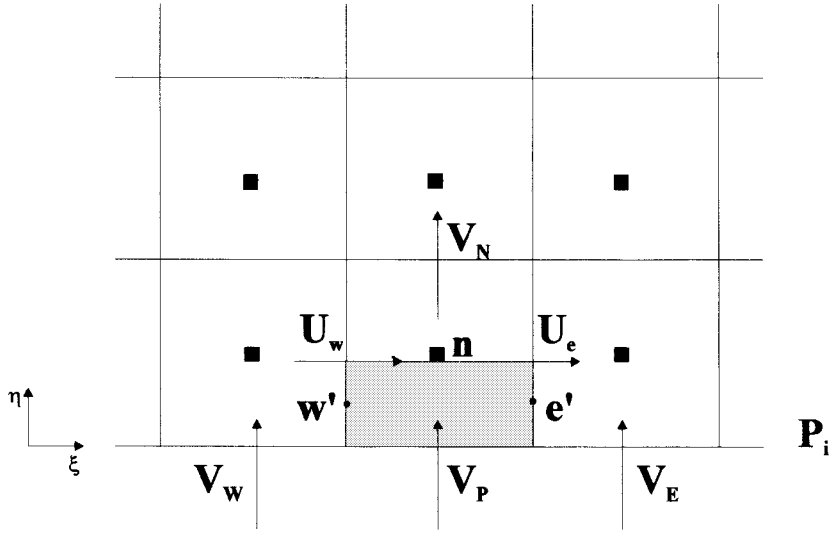

Figure 4. Velocity control volume at the channel entrance.

for the convective and diffusive fluxes at the interfaces, one obtains

$$\phi_P^{n+1} = \left(\frac{A_e \phi_E^{n+1} + A_w \phi_W^{n+1} + A_n \phi_N^{n+1}}{A_p} \right) - \frac{L[\hat{P}^{\phi}]}{A_p} + \frac{\phi_P^n}{1+E} \tag{16}$$

where

$$\begin{aligned} A_e &= -\left(\frac{\rho U}{4}\right)_e + C_{1_{e'}} \overline{\beta}_{e'} \qquad A_w = \left(\frac{\rho U}{4}\right)_w + C_{1w'} \overline{\beta}_{w'} \\ A_n &= (\rho V)_n \left(\frac{1}{2} - \overline{\alpha}_n\right) + 2 C_{4n} \overline{\beta}_n \qquad A_p = A_p^* \left(\frac{1+E}{E}\right) \\ A_p^* &= A_e + A_w + A_n \end{aligned} \tag{17}$$

The term $L[\hat{P}^{\phi}]$ depends on which velocity (u or v) will be corrected. Integrating this term for the Cartesian velocity components, and considering that $P = P(\eta)$ in the south boundary, it becomes

$$L[\hat{P}^{v}] = -\frac{\Delta P}{\Delta \eta} x_{\xi} \Delta \xi \tag{18}$$

$$L[\hat{P}^{u}] = -\frac{\Delta P}{\Delta \eta} y_{\xi} \Delta \xi \tag{19}$$

Multiplying Eq. (16) by x_ξ when $\phi = v$, and by $-y_\xi$ when $\phi = u$, one obtains the following equation for the contravariant velocity V at the channel entrance:

$$V_P = \hat{V}_P - \left(\frac{\gamma \Delta V}{A_P^v} \frac{\Delta P}{\Delta \eta} \right) \tag{20}$$

where

$$\hat{V}_P = A_e^v (v_E x_{\xi P} - u_E y_{\xi P}) + A_w^v (v_W x_{\xi P} - u_W y_{\xi P}) + A_n^v [v_N x_{\xi P} - u_N y_{\xi P}] + \frac{v_P x_{\xi P}}{1 + E} - \frac{u_P y_{\xi P}}{1 + E} \tag{21}$$

At the channel exit the locally parabolic boundary conditions are assumed, that is,

$$\frac{\partial U}{\partial \eta} = \frac{\partial V}{\partial \eta} = 0 \tag{22}$$

Boundary Conditions for Pressure

For incompressible flows, pressure boundary conditions are not required when the velocities are known at the boundary. In this case, the entrance velocity is not known, therefore, pressure needs to be specified. Figure 5 depicts the pressure control volume (continuity control volume) at the entrance. The four contravariant

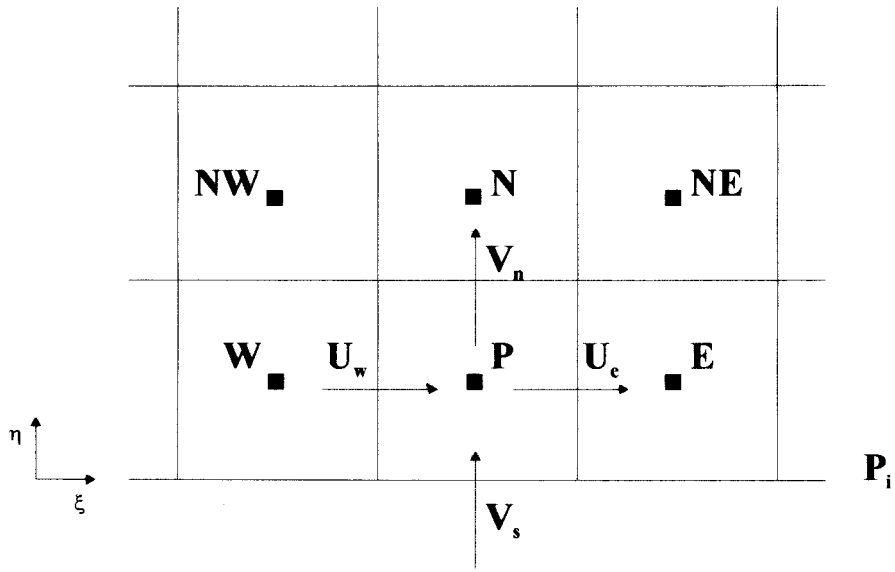

Figure 5. Continuity control volume at the entrance.

components that enter the mass conservation equation for the boundary volume are

$$V_n = \hat{V}_n - \left|\frac{\gamma}{A_P^v}\right|_n (P_N - P_P) + \left|\frac{\beta}{4A_P^v}\right|_n (P_{NE} + P_E - P_{NW} - P_W) \tag{23}$$

$$V_s = \hat{V}_s - \left|\frac{2\gamma}{A_P^v}\right|_s (P_P - P_i) \tag{24}$$

$$U_e = \hat{U}_e - \left|\frac{\alpha}{A_P^u}\right|_e (P_E - P_P) + \left|\frac{\beta}{4A_P^u}\right|_e (P_{NE} + P_N - P_E - P_P) \tag{25}$$

$$U_w = \hat{U}_w - \left|\frac{\alpha}{A_P^u}\right|_w (P_P - P_W) + \left|\frac{\beta}{4A_P^u}\right|_w (P_{NW} + P_N - P_W - P_P) \tag{26}$$

Inserting the above equations into the mass conservation equation, Eq. (14), one obtains the equation for pressure for the boundary volume as

$$A_P P_P = A_e P_E + A_w P_W + A_n P_N + A_{ne} P_{NE} + A_{nw} P_{NW} + B \tag{27}$$

The pressure P_i that appears in Eq. (24) needs to be known. In this article, $P_i = 0$ and $P_i = -0.5\rho\overline{V}_i^2$ are used, where $\overline{V}_i$ is the averaged velocity at the channel entrance. It is clear that the flow near the channel entrance is not irrotational, and the pressure obtained using Bernoulli's equation is not an exact boundary condition. It is, however, much better than using $P_i = 0$. It will be shown that when the pressure at the inlet is made equal to zero, it forces the flow to be of mixed type, and the excess of mass flow, depending on its magnitude, may preclude the capture of the recirculation zone existing at the channel exit.

For the remaining pressure control volumes lying on the other boundaries, the same procedure is employed, introducing, at this time, in the mass conservation equation, the available velocity at that boundary.

NUMERICAL RESULTS

Straight Vertical Channel

The solution of the natural-convection flow in a straight vertical channel is suitable for testing the proposed method regarding to the application of the boundary condition for velocity at the entrance. It also allows one to determine when the flow reversal at the channel exit is suppressed by the incorrect application of the boundary conditions at the inlet. In addition, there are abundant numerical data as well as experimental results for this flow for comparisons. The boundary conditions at the left wall were zero velocity (u and v) and prescribed temperature. Symmetry conditions for velocities and temperature were used at the channel centerline. In the channel entrance the temperature is the same as the ambient temperature (T_o). The velocity is calculated according to Eq. (20) and the

pressure is calculated using Bernoulli's equation. In the channel outlet, locally parabolic conditions were used.

Table 1 shows the results obtained by Aiahara [17], Kettleborough [6], Nakamura et al. [7], and by the method presented in this work. Table 1 also presents the Nusselt number calculated in two ways. Nu_a uses the heat flux calculated at the heated wall and Nu_b uses the difference between the heat flux leaving and entering the channel. If the numerical solution is converged, these Nusselt numbers must be identical. Also shown in Table 1 is the value of the maximum dimensionless streamline in the channel, representing the dimensionless flow rate of the problem. The expressions for the Nusselt number, dimensionless flow rate, and Grashof number are given by Eqs. (28)–(31).

$$\mathrm{Nu}_a = \frac{(1/H)\int_0^H \left[k(\partial T/\partial x)\mid_{x=S/2}\right](S/k)\,dy}{(T_w - T_o)} \tag{28}$$

$$\mathrm{Nu}_b = \frac{(1/H)\int_0^{S/2}\left[(\rho c_p v T)_{y=H} - (\rho c_p v T)_{y=0} + k(\partial T/\partial y)\mid_{y=0}\right](S/k)\,dx}{(T_w - T_o)} \tag{29}$$

$$\Psi^* = \frac{\Psi_{\max}}{\bar{\bar{v}}} \tag{30}$$

$$\mathrm{Gr}_s = \frac{g\bar{\bar{\beta}}(T_w - T_o)S^3}{\bar{\bar{v}}^2} \tag{31}$$

where T_w is the temperature of the heated wall, T_o is the fluid temperature at the channel entrance, and $\Psi_{\max}$ is the maximum value of the streamlines in the channel.

The indices (a)–(c) in Table 1 refer to following boundary conditions used in the parabolic model at the channel entrance, according to Aiahara [17]:

(a) Uniform velocity profile and $P_i = 0$.
(b) Uniform velocity profile and P_i calculated by Bernoulli's equation
(c) Parabolic velocity profile and P_i calculated by $P_i = -27\rho\bar{V}_i^2/35$

Table 1. Nusselt number and dimensionless maximum streamline for the symmetrical vertical channel

	$\mathrm{Gr}_s = 10^2$ and Pr = 0.73			$\mathrm{Gr}_s = 10^4$ and Pr = 0.73		
Reference	Nu_a	Nu_b	ψ^*	Nu_a	Nu_b	ψ^*
[17] (a)	—	0.498	3.530	—	4.180	68.40
[17] (b)	—	0.482	3.410	—	3.780	54.40
[17] (c)	—	0.482	3.410	—	3.600	54.40
[6]	4.750	0.328	0.273	5.500	4.760	73.50
[7]	0.479	0.459	3.140	3.628	3.754	48.00
Present work	0.689	0.689	3.100	3.860	3.860	55.00

Inspecting Table 1, it can be seen that several values of Nu_a and Nu_b do not agree, which suggests that the results, specially the ones from [6], are not well converged, or that the numerical method uses approximated equations that do not force energy conservation at the control-volume level. It is also noted that the results obtained in this work are reasonably close to those of Nakamura et al. [7], which show close values for Nu_a and Nu_b, even though the agreement is, in general, not good. The Nusselt number of Aiahara [17], for boundary condition (*b*) and for $Gr_s = 10^4$, is reasonably close to the result of the present study. However, different Nusselt numbers were obtained for different boundary conditions for pressure, not in agreement with an important conclusion of this work, as will be seen later.

Figure 6 presents numerical results for $P_i = 0$ and for P_i calculated using Bernoulli's equation, compared with the numerical and experimental results of Sparrow et al. [4]. The numerical results of [4] were obtained with the parabolic procedure with constant velocity and P_i equal to zero at the entrance. The experimental results were obtained for water ($Pr = 5.0$), $S/H = 0.0437$, with $S = 0.02$ m and $H = 0.0457$ m. It can be seen that the Nusselt number is insensitive to changes in pressure at the entrance, as well as to the model employed, parabolic or elliptic. The Nusselt and Rayleigh numbers are defined by

$$Nu_s = \frac{\overline{q''}S}{k(T_w - T_o)} \tag{32}$$

$$Ra_s = \frac{g\overline{\overline{\beta}}(T_w - T_o)S^3}{\overline{\overline{\alpha\nu}}} \tag{33}$$

where $\overline{q''}$ is average heat flux at the heated wall.

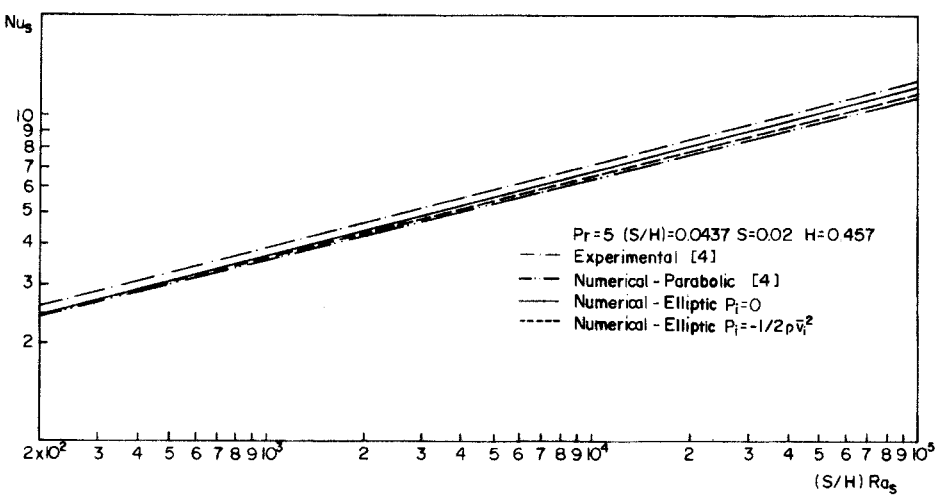

Figure 6. Nusselt number for the vertical channel—left wall isothermal, right wall insulated.

To demonstrate the error in the mass flow calculation due to the inappropriate pressure boundary condition applied at the interface, Table 2 presents the Nusselt number and the mass flow ratio for different values of $(S/H)\,\mathrm{Ra}_s$ and for two pressure conditions at the inlet. Subscripts 1 and 2 refer to pressure equal to zero and pressure calculated via Bernoulli's equation, respectively. It can be seen that the Nusselt number is about the same for both pressures, while the mass flow ratio increases drastically with the increase of the Rayleigh number. Before explaining this behaviour, consider Figures 7 and 8, where the velocity and temperature fields are presented for y/H equal to 0.15, and 0.95, that is, close to

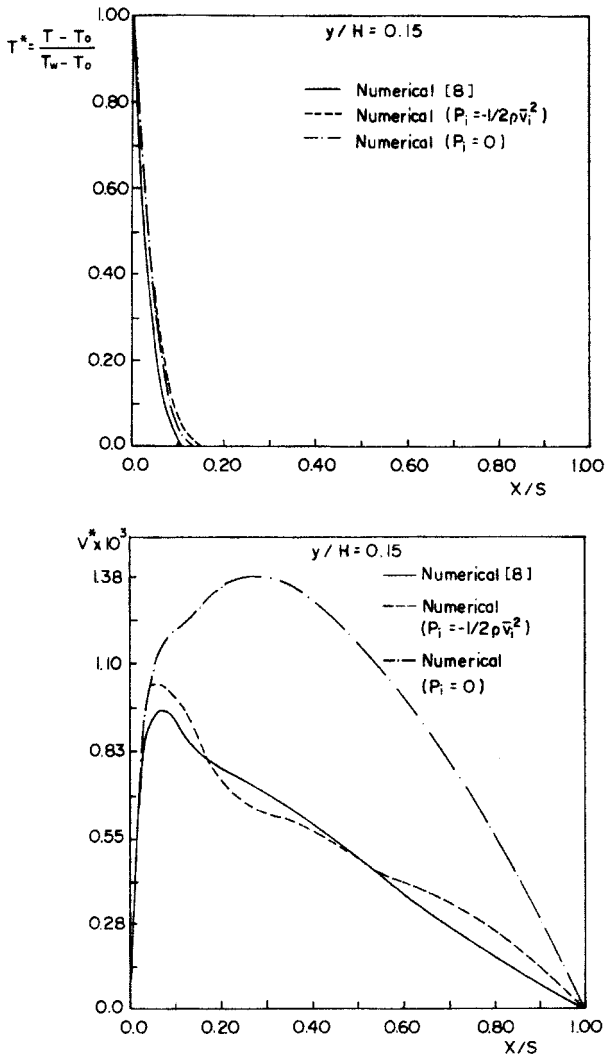

Figure 7. Velocity and temperature profiles—straight channel, $y/H = 0.15$.

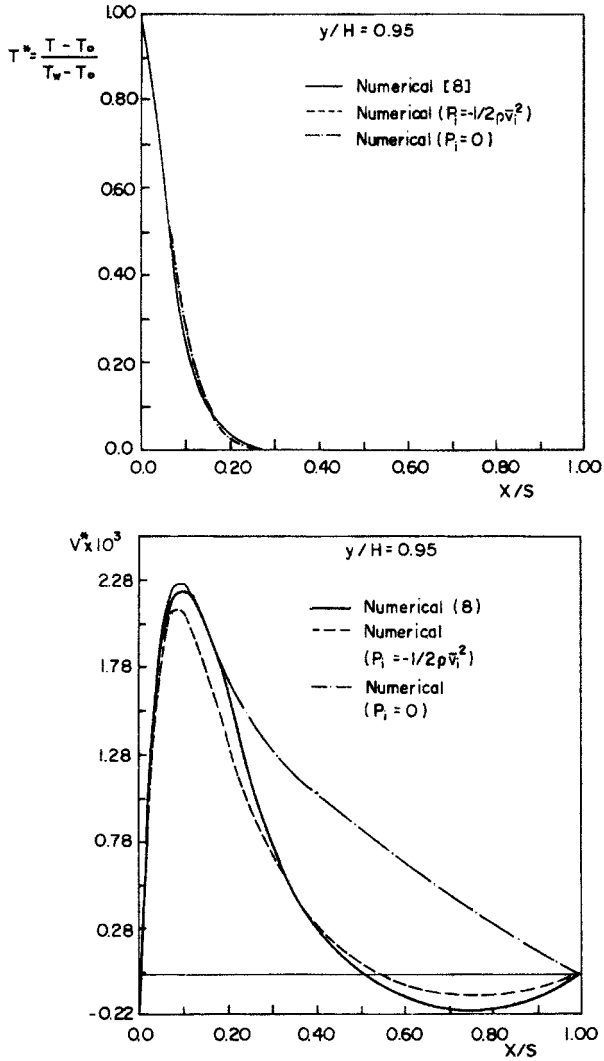

Figure 8. Velocity and temperature profiles—straight channel, $y/H = 0.95$.

the entrance and to the outlet of the channel. The numerical results obtained in [8] and the ones obtained with the elliptic model for $P_i = 0$ and $P_i = -\rho\overline{V}_i^2$, are reported in these figures. It is worth noting that the temperature distribution inside the thermal boundary layer is the same for both boundary conditions for pressure, despite the completely different velocity profiles. The consequence, of course, is that the Nusselt number is almost the same, as already reported in Table 2. The

Table 2. Nusselt number and mass flow ratio for the vertical channel

$(S/H)\,\mathrm{Ra}_s$	10^3	5×10^3	10^4	5×10^4
$\dot{m}_1/\dot{m}_2$	1.063	1.156	1.245	1.697
Nu_{s1}	3.645	5.449	6.473	9.964
Nu_{s2}	3.595	5.342	6.332	9.789
$\mathrm{Nu}_{\mathrm{exp}}$	3.842	5.736	6.816	10.177

dimensionless velocity in Figures 7 and 8 is defined by

$$v^* = \frac{vS}{\bar{\bar{v}}} \tag{34}$$

The reason why completely different velocity profiles give rise to almost identical temperature profiles can be understood by recognizing that the flow in the channel is driven by two different forces. Close to the heated wall, in the thermal boundary layer, the flow is driven by buoyancy, and outside the thermal boundary layer it is driven by pressure forces resulting from the application of the pressure boundary condition at the inlet. Since in the thermal boundary layer the predominant effect is buoyancy, it does not matter which boundary condition for pressure is used in this region. For the rest of the channel cross section, the flow obeys a momentum balance between inertia and viscous drag. To apply $P_i = 0$ at the inlet creates a forced flow, creating, therefore, profiles that overestimate the mass flow rate that would be driven by natural convection. Since this overflow does not alter the thickness of the thermal boundary layer, the heat transfer rate is not affected by the pressure boundary condition at the inlet.

Another interesting point to be considered is the appearance of the recirculation zone close to the insulated wall and near the channel exit. As seen in Figures 7 and 8, the numerical results from [8] and using the present model with pressure calculated via Bernoulli's equation agree well, both revealing the reverse flow at the outlet. The appearance of this recirculation region is easily explained. Since buoyancy pushes the flow toward the hot wall, new fluid needs to be admited through the exit, in order to satisfy mass conservation. For the $P_i = 0$ boundary condition, since the mass flow is overestimated, it is large enough to supply the mass required by the buoyancy effects close to the hot wall, as well as to suppress the reverse flow. For a straight channel the penetration depth of the reverse flow of 0.466 H compares very well with the value of 0.460 H observed experimentally in [8].

L-Shaped Channel

In order to demonstrate the flexibility of the numerical model, the natural-convection flow in an L-shaped channel is solved. This geometry, although not too complex, allows numerical discretization using boundary-fitted coordinates. Figure 9 presents the geometry and the boundary conditions used, and Figure 10 shows the grid employed for $(S/H) = 0.0875$.

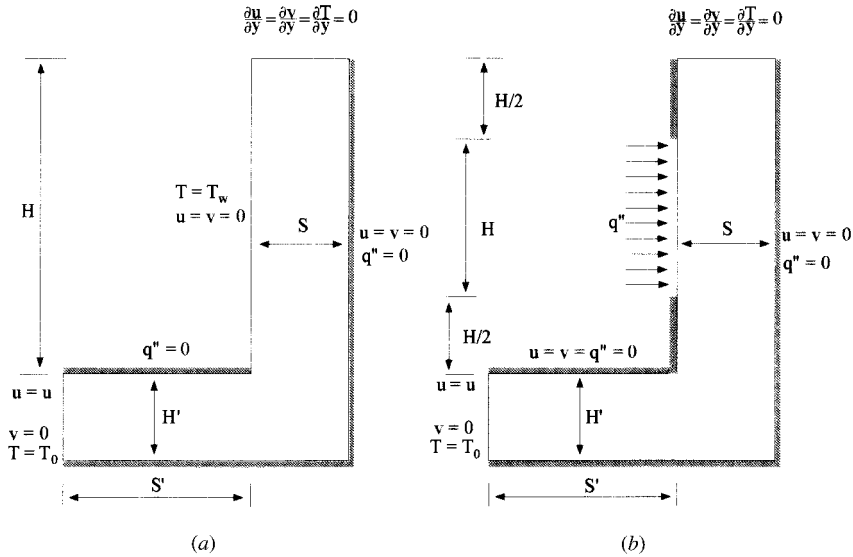

Figure 9. Geometry and boundary conditions for the L-shaped channel.

In all cases H' and S' were maintained constant and equal to 0.1 m and 0.5 m, respectively. The $(S/H)\,\mathrm{Ra}_s$ parameter was changed from 10^3 to 5×10^4. S was kept constant and equal to 0.1 m and H was changed from 1.1428 to 2.228 m. To study the effect of the plate spacing (S) on the heat transfer at the vertical wall, the Ra_H parameter was changed from 10^8 to 8×10^8, keeping H constant and equal to 1.1428 m and changing S from 0.02 to 0.16 m. Table 3 shows the results for $S/H = 0.066$ for several values of $(S/H)\,\mathrm{Ra}_s$, using two boundary conditions for pressure and $\mathrm{Pr} = 5.0$.

Inspecting the mass flow ratios of Table 2 and comparing to those of Table 3 for the L-shaped channel, it can be noted that the straight channel shows the largest mass flow rate ratio. This is because for the L-shaped channel the boundary condition $P_i = 0$ is applied far from the region where the buoyancy effects are important, and therefore its influence diminishes.

Again the values of Nu_s for both boundary conditions for pressure are practically the same, showing similar behavior of the vertical channel. Finally, we analyzed the effect of the horizontal part of the channel in the flow and heat transfer. Since the horizontal part increases the friction losses, such effect causes small values of Nu_s for the L-shaped channel if compared to the straight channel. This occurs because part of the buoyancy forces is spent to compensate for the friction in the horizontal part, decreasing the mass flow rate, which will result in a thicker thermal boundary layer, therefore decreasing the Nusselt number.

Table 4 shows several results for $\mathrm{Pr} = 0.70$ with boundary condition of P_i equal to zero at the channel inlet. For $\mathrm{Pr} = 0.70$ and $(S/H)\,\mathrm{Ra}_s$ larger than 10^3, the calculations were done only for P_i equal to zero at the inlet, because good convergence characteristics were not found when the pressure was prescribed using Bernoulli's equation. Since in the case of the L-shaped channel the mass flow rate

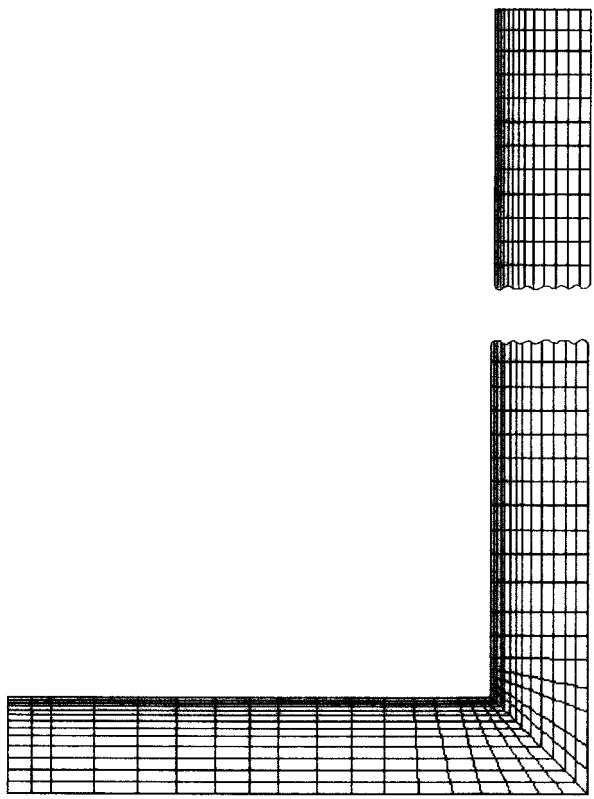

Figure 10. Mesh with (67 × 13) volumes for $(S/H) = 0.08$.

Table 3. Nusselt number and mass flow ratio for the L-shaped channel

$(S/H)\,\mathrm{Ra}_s$	10^3	5×10^3	10^4	5×10^4
Nu_{s1}	2.629	3.980	4.730	7.096
Nu_{s2}	2.610	3.950	4.690	7.037
$\dot{m}_1/\dot{m}_2$	1.030	1.072	1.109	1.270
$\mathrm{Nu}_{\mathrm{exp}}$ (vertical channel)	3.842	5.736	6.816	10.177

Table 4. Nusselt number and mass flow ratio for several relations of (S/H) for the L-shaped channel with $P_i = 0$ at the inlet and Pr = 0.70

(S/H)	$(S/H)\,\mathrm{Ra}_s$	Nu_s	$\dot{m}$
0.0437	10^3	2.654	0.0044
0.0437	5×10^3	3.840	0.0071
0.0437	10^4	4.509	0.0085
0.0437	5×10^4	6.711	0.0146
0.0547	10^3	2.534	0.0035
0.0547	5×10^3	3.676	0.0056
0.0547	10^4	4.330	0.0069
0.0547	5×10^4	6.444	0.0123
0.0666	10^3	2.414	0.0028
0.0666	5×10^3	3.512	0.0046
0.0666	10^4	4.144	0.0056
0.0666	5×10^4	6.171	0.0103
0.0875	10^3	2.230	0.0021
0.0875	5×10^3	3.258	0.0034
0.0875	10^4	3.847	0.0042
0.0875	5×10^4	5.745	0.0080

is not strongly influenced by the type of boundary condition for pressure at the inlet, there were no efforts to elucidate the reason for the divergence. In these results the value of S was kept constant.

Figure 11 shows the streamlines for two Rayleigh numbers, where can be seen the recirculation zones at the channel outlet. For the larger Rayleigh number the fluid penetrates deeper into the channel. The corresponding isotherms are shown in Figure 12, where it is shown that for lower values of the $(S/H)\,\mathrm{Ra}_s$ parameter, the thickness of the thermal boundary layer increases, decreasing the convection heat transfer coefficient. It can be also observed in the horizontal part of the channel that the diffusion of heat upstream to the flow is small for all values of $(S/H)\,\mathrm{Ra}_s$. This means that the temperature at the horizontal part remains constant and equal to the entrance temperature.

Figure 13 presents the local Nusselt number, Nu_L, for four values of Ra_s. It is observed that for the same value of y/H, the largest values of Nu_L occur for the largest value of Ra_s. This is because increasing Ra_s also increases the buoyancy-driven flow rate for the same value of y/H. This leads to an increase in the temperature gradient at the heated wall, increasing the local Nusselt number.

Figure 14 shows the pressure distribution for $(S/H) = 0.0666$, for two values of Ra_s, and for $P_i = 0$ at the entrance. This shows a high pressure gradient close to the entrance region, then decreasing, similar to the hydrodynamic behavior of the developing flow in a channel, reaching its minimum at the beginning of the heating region and then increasing again. It can be seen that the curves near the heated wall (A) in both figures show the above-explained behavior. The other curve (B) in both figures shows an elevation in pressure near the bottom wall. In that region this pressure increase is expected, since kinetic energy is transformed into pressure.

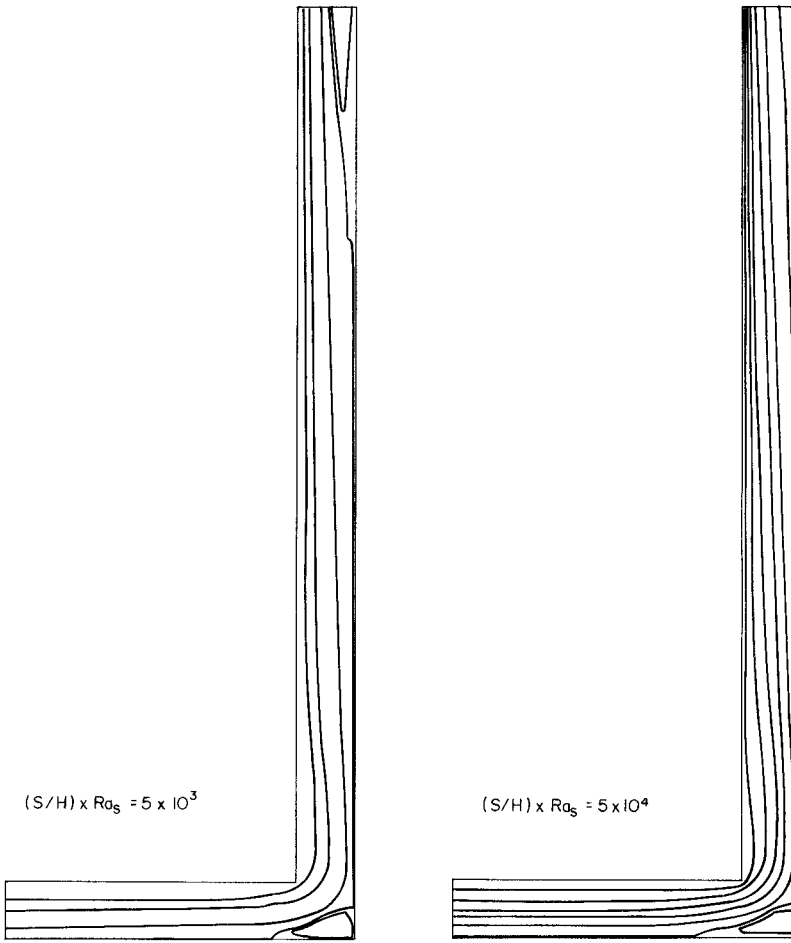

Figure 11. Streamlines for $S/H = 0.0666$ ($S = 0.1$ m, $H = 1.5$ m) and $\mathrm{Pr} = 0.70$. L-shaped channel—one wall isothermal and the other insulated.

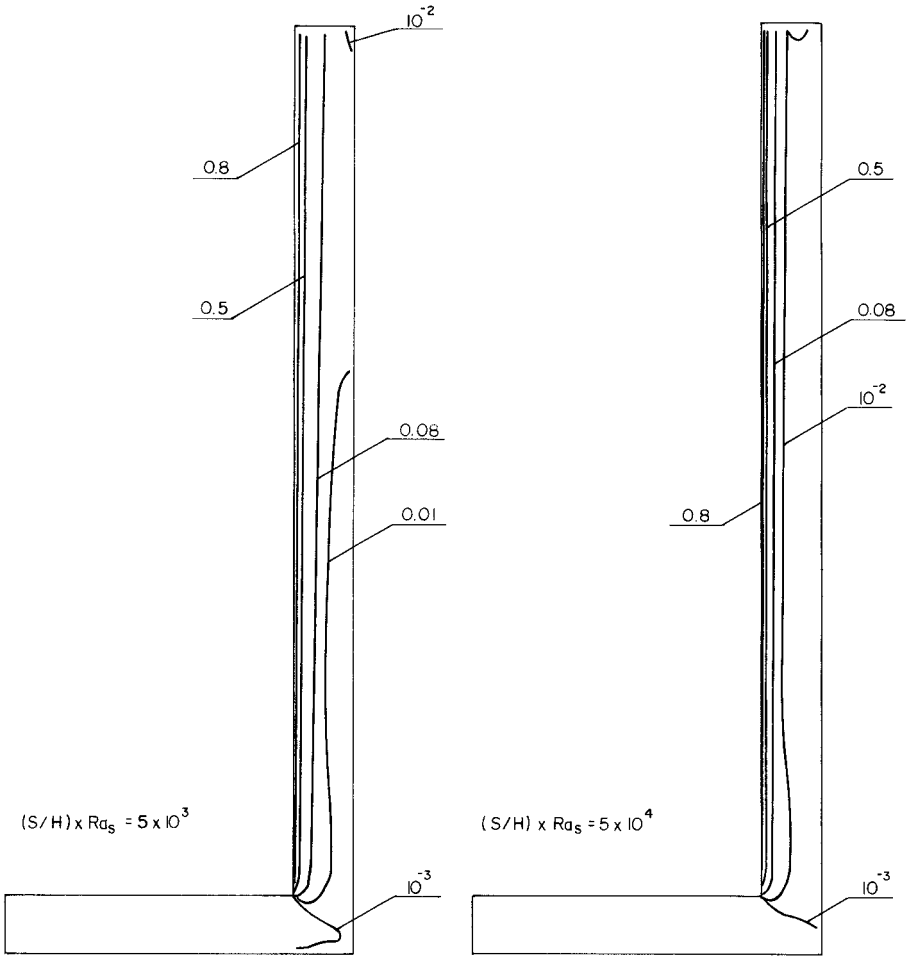

Figure 12. Isotherms for $S/H = 0.0666$ ($S = 0.1$ m, $H = 1.5$ m) and $\mathrm{Pr} = 0.70$. L-shaped channel—one wall isothermal and the other insulated.

Figure 15 presents the average Nusselt number based on the height (H) of the channel, where H was kept constant and equal to 1.1428 m. It is clear by Eq. (35) that Nu_H represents the average heat transfer in the heated wall. Therefore, the effects of the spacing between the plates (S) in the heat transfer rate can be analyzed. The expressions for Nu_H and Ra_H are given by

$$\mathrm{Nu}_H = \frac{\overline{q''} H}{k(T_w - T_o)} \tag{35}$$

$$\mathrm{Ra}_H = \frac{g\bar{\bar{\beta}}(T_w - T_o) H^3}{\bar{\bar{\nu}}\bar{\bar{\alpha}}} \tag{36}$$

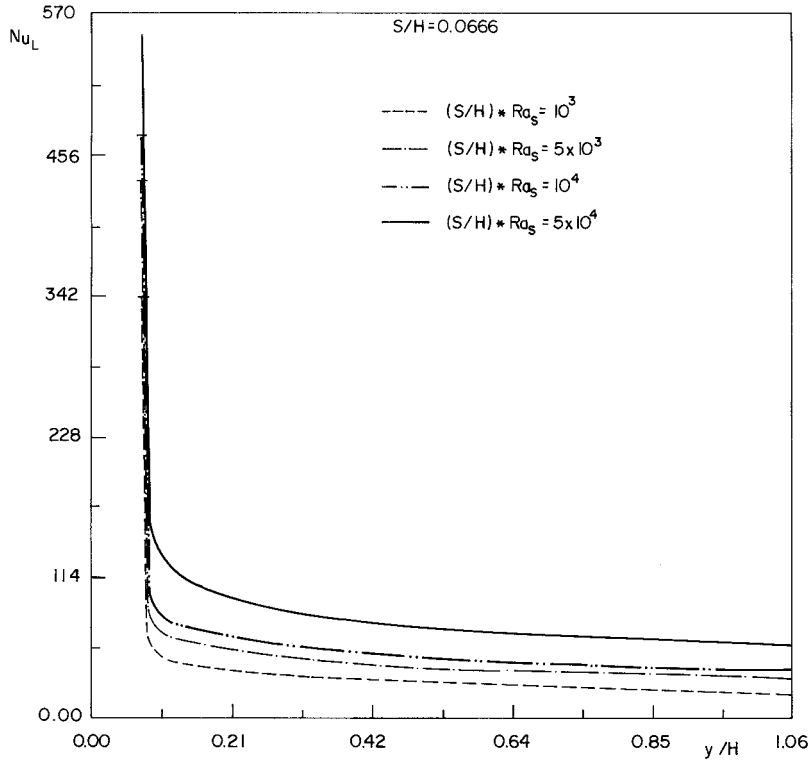

Figure 13. Local Nusselt numbers for $S/H = 0.6666$ ($S = 0.1$ m, $H = 1.5$ m) and $\mathrm{Pr} = 0.70$. L-shaped channel—one wall isothermal and the other insulated.

An interesting comparison is shown in Figure 15, where one can see that the average Nusselt number based on H, for four values of S/H, is always lower than the Nusselt number for the vertical flat late for the same Rayleigh number. This was expected, since in the L-shaped channel the viscous drag reduces the mass flow rate induced by natural convection, lowering the corresponding heat transfer rate. For the L-shaped channel the heat transfer rate is considerably augmented when S is increased from 0.02 to 0.06 m (S/H from 0.0175 to 0.0525). Figure 15 also shows that the maximum heat transfer rate for the L-shaped geometry is achieved for $(S/H) = 0.0525$. This can be explained by the fact that the horizontal part of the channel establishes a flow pattern that fills the full cross-sectional area of the channel. When in the vertical part, there is also flow outside the thermal boundary layer, resembling the flow in a vertical flate plate of fluid with a Prandtl number greater than 1. Calculating the hydrodynamic boundary-layer thickness for natural convection in a vertical flat plate using Eq. (7.20) from [18], the value found will be $(\delta/H) = 0.0486$, very close to $(S/H) = 0.0525$, which presents the largest average heat transfer rate. If (S/H) is increased beyond this value, the thermal boundary

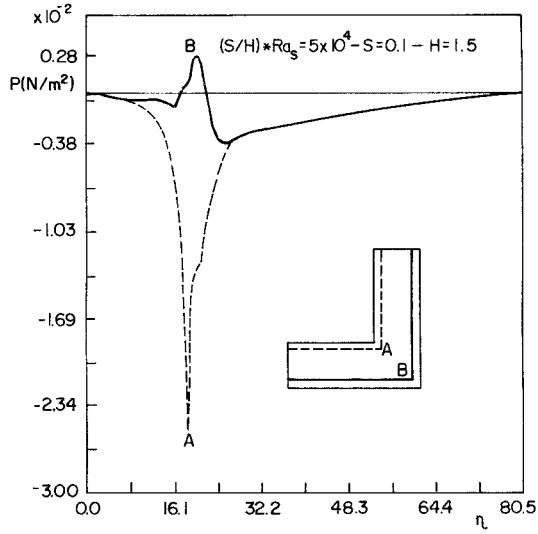

(*a*)

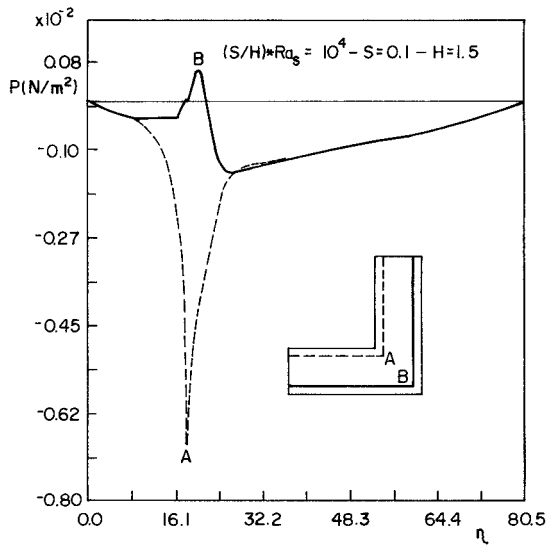

(*b*)

Figure 14. Pressure lines for $S/H = 0.0666$ ($S = 0.1$ m, $H = 1.5$ m) and $\mathrm{Pr} = 0.70$. L-shaped channel—one wall isothermal and the other insulated.

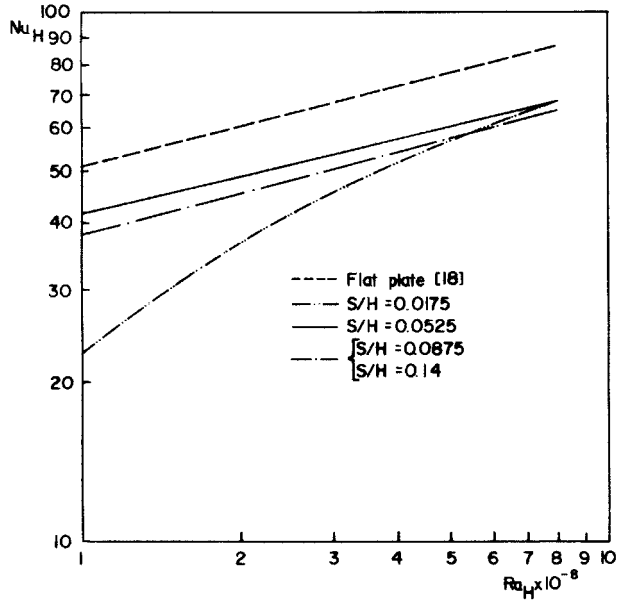

Figure 15. Average Nusselt number based on the channel height for the L-shaped channel.

layer will not fill the channel completely and the cold fluid will decrease the temperature gradient, decreasing the Nusselt number.

As a final calculation for the L-shaped channel, some are results for prescribed heat flux, as indicated in Figure 9, for $(S/H) = 0.133$. The prescribed heat flux was $q'' = 1\,\mathrm{W/m^2}$ and the Rayleigh number based on the heat flux, Ra_{qs}, is defined by

$$\mathrm{Ra}_{qs} = \frac{g\bar{\bar{\beta}}q''S^4}{\bar{\bar{\nu}}\bar{\bar{\alpha}}k} \tag{37}$$

Figure 16 presents the streamlines and Figure 17 the isotherms for two values of $(S/H)\,\mathrm{Ra}_{qs}$. It can be observed that the recirculation region increases when $(S/H)\,\mathrm{Ra}_{qs}$ increases from 10^4 to 5×10^4, as expected, since the condition $P_i = 0$ for the L-shaped channel is now applied far from the region where the buoyancy effects are important, therefore, with less effects in the flow field.

All numerical results were obtained with a convergence criterion in the Cartesian velocity components, u and v, of 10^{-4}. The criterion used [11] finds the maximum and minimum values of the variable in the domain and calculates the range given by the difference between these two values. The calculation stops when the change in the variable from one iteration to another, divided by the range, is less than a specified tolerance for every cell in the domain.

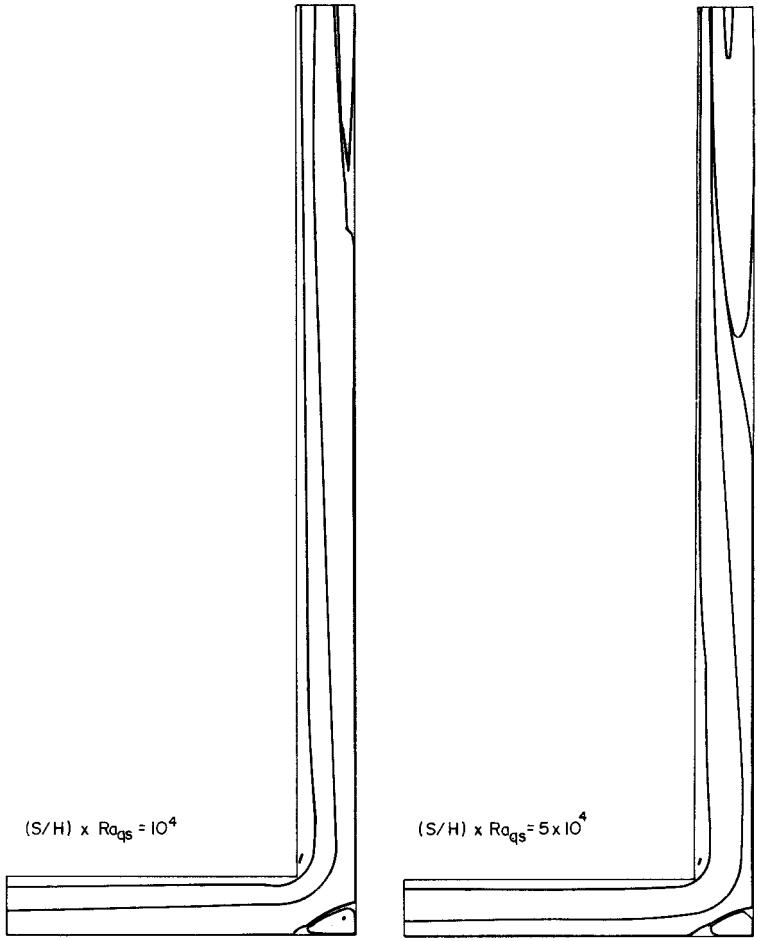

Figure 16. Streamlines for prescribed heat flux. L-shaped channel for $S/H = 0.1333$ ($S = 0.1$ m, $H = 0.75$ m) and Pr = 0.7.

CONCLUSIONS

This article described a methodology for solving elliptic natural-convection flows in open-ended channels. The technique allows the determination of the mass flow rate for a given channel, as opposed to the parabolic approximation that calculates the channel height for a prescribed mass flow rate. Practical problems are of the former class. The article reports a new method for handling the inlet boundary conditions for velocity for open-ended channels, whereby a special equation is created for the inlet velocity, which is then treated as unknown. The key question of the reversal flow at the channel exit, which cannot be analyzed with the parabolic procedure, is also addressed. It is demonstrated that an incorrect pressure applied at the inlet may suppress the reversal flow at the channel outlet.

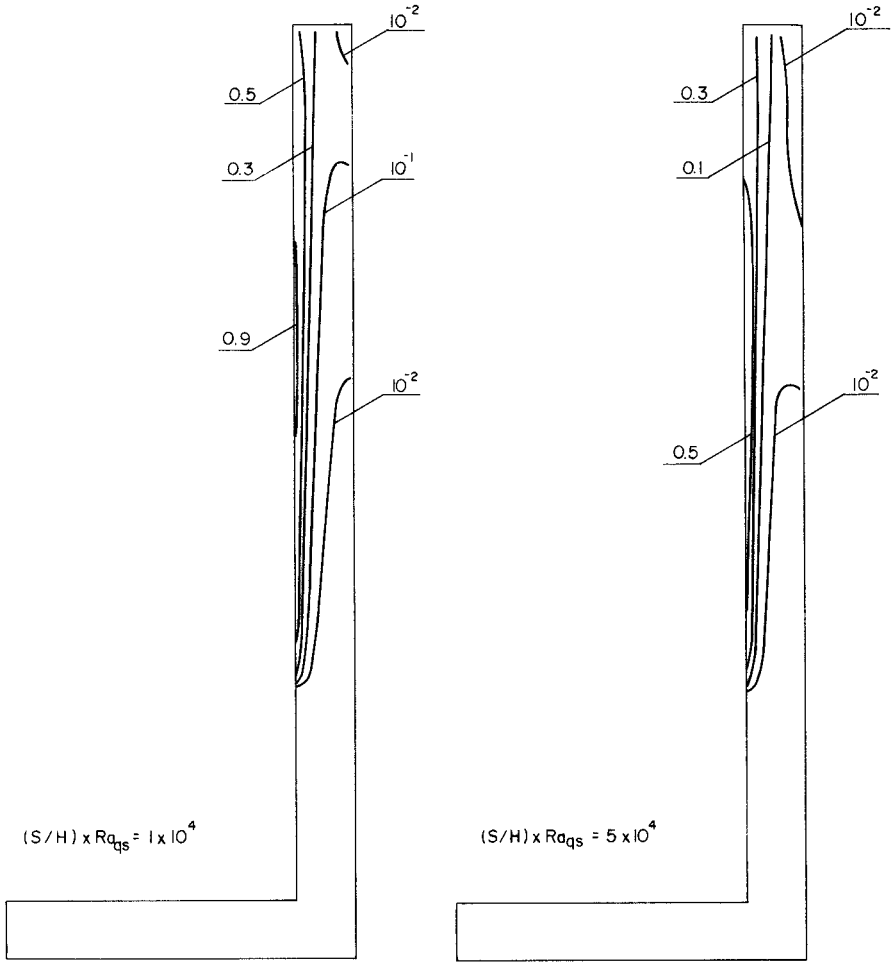

Figure 17. Isotherms for prescribed heat flux. L-shaped for $S/H = 0.1333$ ($S = 0.1$ m, $H = 0.75$ m) and $\mathrm{Pr} = 0.7$.

The heat transfer coefficient, however, are not influenced by the incorrect velocity profile. The explanation for this fact was also given. Calculations for the L-shaped channel were also conducted, demonstrating that the numerical model can be applied to open-ended channels of complex shapes.

REFERENCES

1. J. R. Bodoia and J. F. Osterle, The Development of Free Convection between Vertical Plates, *J. Heat Transfer*, vol. 84, pp. 40–44, 1962.
2. W. Elenbass, Heat Dissipation of Parallel Plates by Free Convection, *Physica*, vol. 9, pp. 1–28, 1942.

3. W. Aung, L. S. Fletcher, and V. Sernas, Developing Laminar Free Convection between Vertical Flat Plates with Asymmetric Heating, *Int. J. Heat Mass Transfer*, vol, 15, pp. 2293–2308, 1972.
4. E. M. Sparrow, G. M. Chrysler, and L. F. Azevedo, Observed Flow Reversals and Measured-Predicted Nusselt Numbers for Natural Convection in a One-Sided Heated Vertical Channel, *J. Heat Transfer*, vol. 106, pp. 325–332, 1984.
5. W. Aung and G. Worku, Developing Flow and Flow Reversal in Vertical Channel with Asymmetric Wall Temperature, *J. Heat Transfer*, vol. 108, pp. 299–304, 1986.
6. C. F. Kettleborough, Transient Laminar Free Convection between Heated Vertical Plates Including Entrance Effects, *Int. J. Heat Mass Transfer*, vol. 15, pp. 883–896, 1972.
7. H. Nakamura, Y. Asako, and T. Naitou, Heat Transfer by Free Convection between Two Parallel Flat Plates, *Numer. Heat Transfer*, vol. 5, pp. 95–106, 1982.
8. A. O. Nieckle and L. F. A. Azevedo, Reverse Flow in One-Sided Heated Vertical Channels in Natural Convection, *Winter Annual Meeting of the ASME*, pp. 71–77, Boston, 1987.
9. D. Naylor, J. M. Floryan, and J. D. Tarasuk, A Numerical Study of Developing Free Convection between Isothermal Vertical Plates, *J. Heat Transfer*, vol. 113, pp. 620–626, 1991.
10. C. R. Maliska, and F. Marcondes, Elliptic Calculations of Natural Convection Flows in Arbitrary Channels, *Proc. 8th Int. Conf. on Laminar and Turbulent Flow*, Swansea, UK, 1993.
11. C. R. Maliska, *Computational Fluid Mechanics and Heat Transfer*, pp. 135–137, 284–297, 185–186 LTC, Rio de Janeiro, Brasil, 1995 (in Portuguese).
12. C. R. Maliska and G. D. Raithby, Calculating Three-Dimensional Fluid Flows Using Nonorthogonal Grids, in C. Taylor, J. A. Johnson, and W. R. Smith, (eds.), *Numerical Methods in Laminar and Turbulent Flow*, Pineridge Press, Swansea, UK, 1983.
13. M. França Filho, Comparative Analysis of Methods for Treating the Pressure-Velocity Coupling Problem, M. Eng. Mec. diss. (in Portuguese), Mechanical Engineering Department, Florianópolis, SC, Brazil, 1991.
14. A. F. C. Silva, C. H. Marchi, M. A. Livramento, and J. L. F. Azevedo, On the Effects of Vectorization for Efficient Computation of Three Dimensional Segregated Finite Volume Solutions, *Proc. XI Mechanical Engineering Conf*, Brazilian Society of Mechanical Science, pp. 109–112, São Paulo, Brazil, 1991.
15. G. D. Raithby and K. E. Torrance, Upstream-Weighted Differencing Schemes and Their Application to Elliptic Problems Involving Fluid Flow, *Comput. Fluids*, vol. 2, pp. 191–206, 1974.
16. G. D. Raithby and G. E. Schneider, Numerical Solution of Problems in Incompressible Fluid Flow: Treatment of the Velocity-Pressure Coupling, *Numer. Heat Transfer*, vol. 2, pp. 417–440, 1979.
17. T. Aiahara, Effects of Inlet Boundary Condition on Numerical Solutions of Free Convection between Vertical Parallel Plates, *Rep. Inst. High Speed Mech.*, Tohoku University, vol. 28, pp. 1–27, 1973.
18. J. P. Holman, *Heat Transfer*, McGraw-Hill, New York, 1973.